# REPORT DOCUMENTATION PAGE

| 1. REPORT DATE (DD-MM-YYYY) June 2015 | 2. REPORT TYPE Technical paper | 3. DATES COVERED (From - To) June 2015-July 2015 |
|---|---|---|

| 4. TITLE AND SUBTITLE | 5a. CONTRACT NUMBER |
|---|---|
| Optimal Runge-Kutta Schemes for High-order Spatial and Temporal Discretizations | In-House |
| | 5b. GRANT NUMBER |
| | 5c. PROGRAM ELEMENT NUMBER |

| 6. AUTHOR(S) | 5d. PROJECT NUMBER |
|---|---|
| Mundis, N., Edoh, A. and Sankaran, V. | |
| | 5e. TASK NUMBER |
| | 5f. WORK UNIT NUMBER Q12J |

| 7. PERFORMING ORGANIZATION NAME(S) AND ADDRESS(ES) | 8. PERFORMING ORGANIZATION REPORT NO. |
|---|---|
| Air Force Research Laboratory (AFMC) AFRL/RQR 5 Pollux Drive Edwards AFB, CA93524-7048 | |

| 9. SPONSORING / MONITORING AGENCY NAME(S) AND ADDRESS(ES) | 10. SPONSOR/MONITOR'S ACRONYM(S) |
|---|---|
| Air Force Research Laboratory (AFMC) AFRL/RQR 5 Pollux Drive Edwards AFB CA 93524-7048 | |
| | 11. SPONSOR/MONITOR'S REPORT NUMBER(S) AFRL-RQ-ED-TP-2015-238 |

| 12. DISTRIBUTION / AVAILABILITY STATEMENT |
|---|
| Distribution A: Approved for Public Release; Distribution Unlimited. |

| 13. SUPPLEMENTARY NOTES |
|---|
| Technical Paper presented at 22nd AIAA Computational Fluid Dynamics Conference; Dallas, TX; 22 June 2015. PA#15303. |

**14. ABSTRACT**

Numerical discretization for unsteady flow simulations can be broken down into spatial and temporal parts which interplay in complex and sometimes unexpected ways. This paper attempts to address how the properties of the spatial discretization help drive the choice of temporal discretization. In addition, it examines methods for higher than second-order accurate time integration using L-stable singly-diagonally-implicit (ESDIRK) Runge-Kutta methods.[1, 2] Von Neumann analysis is used to examine the theoretical effects of different spatial/temporal discretization combinations. The predictive nature of the von Neumann analysis is then validated through the exploration of the convection of acoustic waves in one dimension and an isentropic vortex in three dimensions. Is is shown that the computational results follow the expected trends taking the von Neumann analysis of the schemes into account. This work highlights that, for unsteady problems, both dissipation and dispersion errors must be accounted for when selecting optimal Runge-Kutta time integrators.

**15. SUBJECT TERMS**

| 16. SECURITY CLASSIFICATION OF: | | | 17. LIMITATION OF ABSTRACT | 18. NUMBER OF PAGES | 19a. NAME OF RESPONSIBLE PERSON Venke Sankaran |
|---|---|---|---|---|---|
| a. REPORT Unclassified | b. ABSTRACT Unclassified | c. THIS PAGE Unclassified | SAR | 21 | 19b. TELEPHONE NO (include area code) 661-275-5534 |

# Optimal Runge-Kutta Schemes for High-order Spatial and Temporal Discretizations

Nathan L. Mundis[*]    Ayaboe K. Edoh[†]    Venkateswaran Sankaran[‡]

*ERC, Inc.,*

†*University of California – Los Angeles,*

‡*Air Force Research Laboratory,*

*Edwards Air Force Base, California 93524*

**Numerical discretization for unsteady flow simulations can be broken down into spatial and temporal parts which interplay in complex and sometimes unexpected ways. This paper attempts to address how the properties of the spatial discretization help drive the choice of temporal discretization. In addition, it examines methods for higher than second-order accurate time integration using *L*-stable singly-diagonally-implicit (ES-DIRK) Runge-Kutta methods.[1,2] Von Neumann analysis is used to examine the theoretical effects of different spatial/temporal discretization combinations. The predictive nature of the von Neumann analysis is then validated through the exploration of the convection of acoustic waves in one dimension and an isentropic vortex in three dimensions. Is is shown that the computational results follow the expected trends taking the von Neumann analysis of the schemes into account. This work highlights that, for unsteady problems, both dissipation and dispersion errors must be accounted for when selecting optimal Runge-Kutta time integrators.**

## I.   Introduction

The use of high-order spatial discretizations is becoming common for complex, unsteady flow simulations. However, the accuracy of time integration methods has not kept pace with advances in spatial accuracy and second-order accurate methods in time remain the norm. This limit in temporal accuracy is primarily a result of the second Dahlquist barrier which states that no *A*-stable, implicit linear multistep method of order of accuracy greater than two exists.[3] As such, for higher-order time integration, multistage methods, such as Runge-Kutta (RK) methods must be utilized. Since multistage methods require multiple residual calculations for a given time step, they seem immediately to be poor choices. However, Wang and Mavriplis have shown, for the same fourth-order, diagonally implicit Runge-Kutta method investigated in this work, that high accuracy requirements favor higher-order time integration using larger time steps versus lower-order time integration with smaller time steps.[4] In the present work, an attempt is made to generalize these results to a broader class of high-order temporal and spatial schemes. Specifically, von Neumann analysis is performed to categorize the dissipation and dispersion properties of several candidate schemes and to discern their comparative strengths and weaknesses. The results of the von Neumann analysis are then shown to extend readily to real world flows in the form of a convecting isentropic vortex.

Explicit Runge-Kutta time integrators may seem to offer a cheaper route to high-order temporal accuracy, and, indeed, are widely used for that purpose. However, explicit methods are limited by stability restrictions that make them unsuitable for stiff problems such as flows with disparate physical timescales. Examples include low Mach number flows, which are particularly challenging when the low-Mach regions occur simultaneously with transonic and supersonic regions. In addition, timescale stiffness occurs in high Reynolds number boundary layers, wherein the close cell spacing in the wall-normal direction introduces severe time-step restrictions that render the evolution of large-scale features such as vortices quite inefficient. Preconditioning methods have been developed to address the low-Mach limit,[5,6,7,8,9,10,11,12] aspect ratio convergence degradation,[5,8] and both the low and high Reynolds number limits,[8,9] among others. Moreover, for preconditioned unsteady solutions in physical time, a dual-time stepping paradigm must

---

[*]Research Scientist, AIAA Member; email: nathan.mundis.ctr@us.af.mil.

[†]Ph.D. Candidate, AIAA Student Member; ayaboe.edoh.ctr@us.af.mil.

[‡]Senior Scientist, AIAA Senior Member; email: venkateswaran.sankaran@us.af.mil.

be used[13] where each physical time-step is treated as an instantaneously steady solution in pseudo time. In this way, preconditioning can be used at the pseudo-time level and the accuracy of the physical-time solution is retained. In fact, it has also been shown that the preconditioning formulation enables the definition of the artificial dissipation terms to be cast in such a way that accuracy is preserved for stiff problems.[7] Therefore, for generality and because of interest in multi-speed and high Reynolds number, wall-bounded flow regimes, a dual-time framework is adopted in the present work.

In the present work, von Neumann analysis[14] is used systematically to examine the stability behavior and the numerical dissipation and dispersion errors of general combinations of high-order spatial and temporal discretizations. Different Runge-Kutta time integrators are applied to central-difference spatial schemes with added artificial dissipation terms. The overall objective is to gain better understanding of the accuracy of these schemes and to determine optimal choices of spatial and temporal discretizations for practical Euler and Navier-Stokes simulations at all speeds and Reynolds numbers.

The following section describes the governing equations and spatial and temporal discretizations. Then, the theory behind von Neumann analysis as well as its results in the form of dissipation and dispersion error analyses are presented. Next, results of the convection of acoustic waves in one dimension and an isentropic vortex in three dimensions are cataloged. Finally, important conclusions as well as the path forward from the present work are summarized.

## II.   Governing Equations

Consider the Navier-Stokes equations written using dual-time stepping with both physical- and pseudo-time steps, as follows:

$$\frac{\partial \mathbf{Q}}{\partial \tau} + \frac{\partial \mathbf{Q}}{\partial t} + \frac{\partial \mathbf{F}_i}{\partial x_i} = \frac{\partial \mathbf{V}_i}{\partial x_i} + \mathbf{H} \tag{1}$$

where the first term is the pseudo-time derivative, the second term is the physical-time derivative, the third term is the convective term using the inviscid fluxes $\mathbf{F}_i$, the fourth term is the derivative of the viscous fluxes $\mathbf{V}_i$, and the last term $\mathbf{H}$ is a source term. In the present work, $\mathbf{H} = 0$ for all of the solutions and analyses presented: it is included above for thoroughness. The vector of conserved variables is given by $\mathbf{Q} = [\rho \quad \rho u_i \quad \rho e_0]^T$, while the inviscid fluxes are given by $\mathbf{F}_i = [\rho u_i \quad \rho u_i u_j + p\delta_{ij} \quad u_i \rho h_0]^T$ where $h_0 = e_0 + \frac{p}{\rho}$. To aid in analysis, the Navier-Stokes equations are frequently written in quasi-linear form as follows:

$$\frac{\partial \mathbf{Q}}{\partial \tau} + \frac{\partial \mathbf{Q}}{\partial t} + \underline{\mathbf{A}} \frac{\partial \mathbf{Q}}{\partial x_i} = \frac{\partial \mathbf{V}_i}{\partial x_i} + \mathbf{H} \tag{2}$$

where $\underline{\mathbf{A}} = \frac{\partial \mathbf{F}_i}{\partial \mathbf{Q}} = \underline{\mathbf{M}} \underline{\mathbf{\Lambda}} \underline{\mathbf{M}}^{-1}$, with $\underline{\mathbf{M}}$ and $\underline{\mathbf{M}}^{-1}$ being the right and left eigenvectors, respectively, and $\underline{\mathbf{\Lambda}}$ being the matrix of eigenvalues, $\lambda = \{u_i + c, u_i, u_i - c\}$. The Navier-Stokes equations can also be rendered in a residual formulation as follows:

$$\frac{\partial \mathbf{Q}}{\partial \tau} + \frac{\partial \mathbf{Q}}{\partial t} + \mathbf{R}_s(\mathbf{Q}) = 0 \tag{3}$$

where $\mathbf{R}_s = \frac{\partial \mathbf{F}_i}{\partial x_i} - \frac{\partial \mathbf{V}_i}{\partial x_i} - \mathbf{H}$ is the complete spatial residual of the chosen spatial discretization.

### A.   Spatial Discretization

In the present work, the convection term will be discretized using central differences with second, fourth, and sixth orders of accuracy, as follows:

$$\left. \frac{\partial \Upsilon_j}{\partial x_i} \right|_{II} = \frac{\Upsilon_{j+1} - \Upsilon_{j-1}}{2\Delta x_i} \tag{4}$$

$$\left. \frac{\partial \Upsilon_j}{\partial x_i} \right|_{IV} = \frac{-\Upsilon_{j+2} + 8\Upsilon_{j+1} - 8\Upsilon_{j-1} + \Upsilon_{j-2}}{12\Delta x_i} \tag{5}$$

$$\left. \frac{\partial \Upsilon_j}{\partial x_i} \right|_{VI} = \frac{\Upsilon_{j+3} - 9\Upsilon_{j+2} + 45\Upsilon_{j+1} - 45\Upsilon_{j-1} + 9\Upsilon_{j-2} - \Upsilon_{j-3}}{60\Delta x_i} \tag{6}$$

where $\Upsilon$ could be $\mathbf{F}_i$ or $\mathbf{Q}$ depending on the form of the equations.

As is well known, if central differences are used for the convection term, it is generally necessary to add a dissipative term to the Navier-Stokes equations to ensure convergence. In the present work, scalar artificial dissipation is

utilized for this purpose as follows:

$$\mathbf{R}_s = \frac{\partial \mathbf{F}_i}{\partial x_i} - \varepsilon_\eta \parallel \lambda \parallel \frac{\partial^\eta \mathbf{Q}}{\partial x_i^\eta} - \frac{\partial \mathbf{V}_i}{\partial x_i} - \mathbf{H} \tag{7}$$

where $\eta$ is an even number corresponding to one more than the order of accuracy inherent in the artificial dissipation term, $\parallel \lambda \parallel = |u_i| + c$ is the maximum inviscid eigenvalue of the pseudo-linear equations where $u_i$ is the velocity in the direction in which the derivative is being taken, and $\varepsilon_\eta$ is a scaling factor appropriate for the chosen order of accuracy:

$$\varepsilon_{II} = \frac{\Delta x_i}{2}, \quad \varepsilon_{IV} = -\frac{\Delta x_i^3}{12}, \quad \varepsilon_{VI} = \frac{\Delta x_i^5}{60}.$$

Typically, $\frac{\partial^\eta \mathbf{Q}}{\partial x_i^\eta}$ is discretized using a second-order accurate finite difference formula of the $\eta$-degree derivative. The order of accuracy of the artificial dissipation term is given by the power of the $\Delta x_i$ in the $\varepsilon_\eta$ coefficients.

## B.   Preconditioning

To accelerate the convergence of the system for a variety of physical and computational phenomena that can cause the system to become stiff, preconditioning can be used. Phenomena that increase the stiffness of the system include, but are not limited to, low Mach number, high aspect-ratio cells, low and high Reynolds number, and high-frequency unsteadiness. Preconditioning techniques to address all of these phenomena have already been developed in the literature.[6,7,5,8,9] In addition, the source term $\mathbf{H}$ can also cause the system to become stiff. Preconditioning to address source term stiffness could also be developed along similar lines, depending on the nature of the source term.

## C.   Temporal Discretizations

Thus far, the focus has been on the spatial discretization. In this section, the discretization of the temporal derivatives is considered. Both physical- and pseudo-time derivatives are discretized with Runge-Kutta methods. Consider the flow equations written in residual form as given above, but repeated for convenience:

$$\frac{\partial \mathbf{Q}}{\partial \tau} + \frac{\partial \mathbf{Q}}{\partial t} = -\mathbf{R}_s(\mathbf{Q}).$$

First, the physical time derivative will be discretized as follows:

$$\frac{\partial \mathbf{Q}}{\partial \tau} + \frac{\mathbf{Q}^m - \mathbf{Q}^n}{\Delta t} = -\sum_{j=1}^{s} a_{mj} \mathbf{R}_s(\mathbf{Q}^j) \tag{8}$$

where $n$ is the physical-time step index, $m$ is the physical-time Runge-Kutta stage index, and $s$ is the number of RK stages. The residual weights $a_{mj}$ are drawn from the Butcher tableau for the chosen physical-time method. Each stage occurs at a discrete fraction of the time step, which is given by the left column of $c_j$ in the Butcher tableau. If the Runge-Kutta method is fully-implicit, the summation in equation (8) must truly range over all stages and the unknown stage values must all be solved simultaneously. However, if a diagonally-implicit Runge-Kutta method is used instead, this sum proceeds only through the current stage because the Butcher tableau for such a method is lower triangular. Additionally, since current-stage values depend only on past-stage values, only the current stage value is unknown during each stage evaluation. Thus, subsequent stages can be solved sequentially. For this reason, only diagonally-implicit Runge-Kutta methods are considered in the present work. The updated solution at the end of the physical-time step is calculated from the already-solved stage values as follows:

$$\mathbf{Q}^{n+1} = \mathbf{Q}^n - \Delta t \sum_{j=1}^{s} b_j \mathbf{R}_s(\mathbf{Q}^j) \tag{9}$$

where the $b_j$ are taken from the bottom row of the Butcher tableau. All the schemes considered herein are "stiffly accurate" meaning the row of $b_j$ is identical to the last row of $a_{mj}$. This property means that the result of the last stage is also the result at the end of the time step and is considered to be an essential property in the solution of stiff equations.[15] The Butcher tableaux for all of the Runge-Kutta methods mentioned herein are given in Appendix A.

The pseudo-time derivative can be discretized either implicitly with BDF1 or explicitly with forward-Euler or an explicit Runge-Kutta method; in the present work, Jameson's explicit fourth-order Runge-Kutta is used for pseudo-time stepping. Choice of the pseudo-time discretization has little impact on solution accuracy and primarily impacts solution efficiency. As such the precise choice of pseudo-time method will not be discussed further.

American Institute of Aeronautics and Astronautics

# III.   Von Neumann Analysis

One of the main goals of this analysis is to examine the characteristics of different time integrators when applied to specified spatial discretizations. For linear equations, von Neumann analysis can not only give indications of the stability of a given combination of spatial and temporal schemes, it can also indicate how the numerical solution will differ from the exact solution. The output of von Neumann analysis includes both of the following: which wave numbers are damped and by how much per time step (dissipation error) and how the wave speeds at various wave numbers correspond to the exact wave speeds at those same wave numbers (dispersion error). The following sections describe both how von Neumann analysis can be applied to the implicit Runge-Kutta time integrators and the results for different combinations of the spatial and temporal discretizations discussed above. It should be noted that although von Neumann analysis is technically only valid for linear equations, it has been assumed that the insights garnered from it are at least approximately applicable to the non-linear Euler equations. It should also be noted that the method used in this paper to perform von Neumann analysis is specifically tailored for equations that can be treated numerically as systems of ordinary differential equations.

## A.   Theory

To derive von Neumann analysis, begin with the scalar equation:

$$\frac{\partial q}{\partial t} + \lambda \frac{\partial q}{\partial x} - \varepsilon_\eta |\lambda| \frac{\partial^\eta q}{\partial x^\eta} = 0 \tag{10}$$

Replace $q$ with its Fourier representation at spatial points $j$ and temporal points $n$:

$$
\begin{aligned}
q_j^n &= \sum_{k=1}^{\infty} \hat{q}_k e^{\omega t} e^{ikx} \\
q_{j-1}^n &= \sum_{k=1}^{\infty} \hat{q}_k e^{\omega t} e^{ik(x-\Delta x)} \\
q_{j+1}^n &= \sum_{k=1}^{\infty} \hat{q}_k e^{\omega t} e^{ik(x+\Delta x)} \\
q_j^{n+1} &= \sum_{k=1}^{\infty} \hat{q}_k e^{\omega(t+\Delta t)} e^{ikx} \\
etc&.
\end{aligned}
\tag{11}
$$

Even though an infinite summation is shown above, a given resolution can in fact only resolve a finite number of modes. Taking $\hat{q}_k = 1$ (because it turns out that all the $\hat{q}_k$ will cancel for linear systems) and using the above substitutions in equation (10) with the spatial part discretized using central differences, the following spatial eigenvalue contributions are obtained for the flux contribution:

$$
\begin{aligned}
Z(\theta)_{II} &= -\frac{i}{\Delta x} \lambda \sin \theta \\
Z(\theta)_{IV} &= -\frac{i}{6\Delta x} \lambda \left[ 8 \sin \theta - \sin 2\theta \right] \\
Z(\theta)_{VI} &= -\frac{i}{30\Delta x} \lambda \left[ 45 \sin \theta - 9 \sin 2\theta + \sin 3\theta \right] \\
Z(\theta)_{VIII} &= -\frac{i}{140\Delta x} \lambda \left[ 224 \sin \theta - 56 \sin 2\theta + \frac{32}{3} \sin 3\theta - \sin 4\theta \right]
\end{aligned}
\tag{12}
$$

where $\theta = k\Delta x$ is the wave number which ranges from $[-\pi, \pi]$. For the artificial dissipation contribution, the following spatial eigenvalue contributions are obtained for second-order accurate $\eta$-derivatives:

$$Z(\theta)_\eta = \zeta_\eta \frac{|\lambda|}{2} (-1)^{\frac{\eta}{2}-1} (2\cos\theta - 2)^\eta \tag{13}$$

where, as above, $\eta$ is an even number corresponding to one more than the order of accuracy inherent in the artificial dissipation term and:

$$\zeta_{II} = \frac{1}{\Delta x}, \quad \zeta_{IV} = \frac{1}{6\Delta x}, \quad \zeta_{VI} = \frac{1}{30\Delta x}, \quad \zeta_{VIII} = \frac{1}{140\Delta x}$$

which mirror the coefficients of the convective terms above. It should be noted that the convective contribution is purely imaginary and the diffusive contribution is purely real. The total spatial eigenvalues are the the sum of the convective term for the order of accuracy chosen and the diffusive term for the order of accuracy chosen.

Once the eigenvalues for the spatial discretization are found, they are then used in the time discretization. As noted previously, all of the time discretizations considered herein can be written as Runge-Kutta schemes. The amplification

factor for the combined spatial-temporal scheme can be calculated as follows for a general RK scheme with a Butcher tableau as referenced in the previous section:

$$q^{n+1} = q^n + \Delta t \sum_{i=1}^{s} b_i k_i \tag{14}$$

where the $k_i$ are the stage values found as follows for equation (10), above:

$$k_i = Z(\theta) q^{n+c_i \Delta t} = Z(\theta) \left( q^n + \sum_{j=1}^{s} a_{ij} k_j \right). \tag{15}$$

where $c_i$ is the fraction of the time step at which the current stage is occurring, as given by the left column of a Butcher tableau, discussed above. By rearranging this equation into the following form:

$$(1 - a_{ii}Z) k_i - Z \left( \sum_{j=1, i \neq j}^{s} a_{ij} k_j \right) = q^n Z \tag{16}$$

it becomes clear that it can be rewritten as a linear system as follows:

$$\begin{bmatrix} 1 - a_{11}Z & -a_{12}Z & \cdots & -a_{1s}Z \\ -a_{21}Z & 1 - a_{22}Z & \cdots & -a_{2s}Z \\ \vdots & \vdots & \ddots & \vdots \\ -a_{s1}Z & -a_{s2}Z & \cdots & 1 - a_{ss}Z \end{bmatrix} \begin{Bmatrix} k_1 \\ k_2 \\ \vdots \\ k_s \end{Bmatrix} = q^n \begin{Bmatrix} Z \\ Z \\ \vdots \\ Z \end{Bmatrix} \tag{17}$$

This equation is then solved for $k_i$, which are then combined in equation (14) as follows to find the amplification factor $G(Z)$ as a function of the complex spatial eigenvalues as follows:

$$G\left(Z(\theta)\right) = \frac{q^{n+1}}{q^n} = \Delta t \left( 1 + \sum_{i=1}^{s} b_i k_i \right). \tag{18}$$

When the magnitude of $G(Z)$ is found, $|G|$ gives the amplification of the scheme for a given spatial eigenvalue or wave number. When $|G| > 1$, the scheme is unstable as the values are amplified. When $|G| < 1$, the scheme is stable as the values are dissipated. Ideally $|G| \leq 1$, but also very close to one for all wave numbers except the highest wave number. When the angle formed by the real and imaginary parts of $G(Z)$ is found and divided by the corresponding wave speed $-\lambda\theta$ for the given scheme, the phase error of the overall scheme is found, as follows:

$$\phi_e = \frac{\tan^{-1} \left( \frac{Im(G)}{Re(G)} \right)}{-\lambda\theta}. \tag{19}$$

The phase error $\phi_e$ indicates what proportion of the exact wave speed the wave, corresponding to a given wave number, is traveling. When $\phi_e > 1$ the wave is moving faster than it should and when $\phi_e < 1$ the wave is moving slower than it should. Ideally, $\phi_e = 1$ at all wave numbers.

## B.   Results

The results of the von Neumann analyses can clarify how the various spatial and temporal discretization combinations behave. For instance, when progressively higher-order central differences are used, the spatial eigenvalues can be observed to stay closer to their exact values for a larger range of wave numbers. This trend is expressed mainly by shifting the location at which the extreme values occur to a higher wave number and increasing the magnitude of that extreme, as can be seen in Figure (1(a)). In other words, as the order of accuracy increases, the eigenvalues for the lower wave numbers become more and more linear. Even though the extreme value of the eigenvalues increases with increasing order of accuracy, the condition number for different Mach numbers remains the same no matter the order of accuracy of the spatial scheme because the spatial eigenvalues scale equally for all wave numbers.

The addition of artificial dissipation to the spatial discretization adds a negative real part to the spatial eigenvalues. As the order of accuracy of the artificial dissipation term increases, the magnitude of this added real term increases

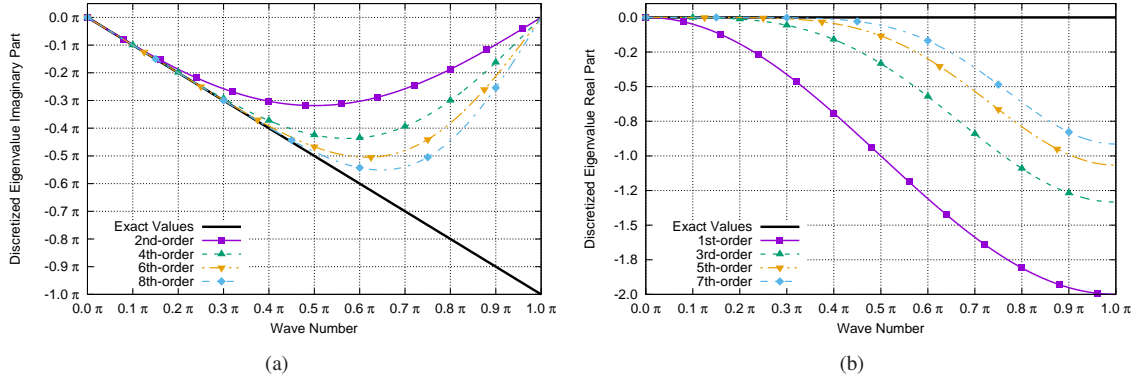American Institute of Aeronautics and Astronautics

Figure 1: (a) The imaginary part of the spatial eigenvalues for central differences of second, fourth, sixth, and eighth order, and (b) the real part of the spatial eigenvalues for artificial dissipation of first, third, fifth, and seventh order

more slowly (indicating better accuracy), as can be seen in Figure (1(b)). It should be noted that since scalar dissipation is used, all three waves experience the same amount of dissipation for a given wave number. It should be obvious that this can cause problems at low Mach numbers. The fastest wave has a ratio of dissipation to convection of one at the mid-wave number for second-order central differences and first-order artificial dissipation, whereas the slowest wave, which scales like Mach number, has a ratio of convection to dissipation of $\frac{1}{M}$ at the the mid-wave number. It should also be noted that the $CFL$ number acts as a scaling factor; thus, if the $CFL$ number doubles, both the real and imaginary parts of all three sets of spatial eigenvalues double. For this reason, it is sufficient only to examine the spatial eigenvalue trends at a single $CFL$ number.

To add the impact of the temporal discretization to the von Neumann analysis, the complex parametric curves describing the spatial eigenvalues (with the wave number being the parameter) are overlaid on the contour map of the amplification factor in the complex plane for the chosen temporal scheme. The complex valued amplification factors that correspond to the spatial eigenvalue curves are used to find both the the magnitude of the growth factor, i.e. one minus the numerical dissipation of the overall scheme, as well as the phase error of the overall scheme, as a function of the wave number. Figures (2) and (3) plot the magnitude of the amplification factor versus the wave number for BDF1 and ESDIRK4 temporal discretizations. In all cases, only the most quickly propagating wave is shown. Subfigure (a) charts this comparison using second-, fourth-, sixth-, and eighth-order central differences with no artificial dissipation, while subfigure (b) plots the same series for spatial schemes with overall accuracy of first through sixth orders. As can be seen, somewhat unexpectedly, higher-order central differences are actually more dissipative in the absence of artificial dissipation. This result occurs because the growth factor in the imaginary direction (y-axis) decreases fairly rapidly for BDF1. While the results for ESDIRK4 exhibit this same trend, it is important to note the scale on the y-axis of the ESDIRK4 subplot (a) (i.e. dissipation is negligible).

Examining subfigure (b) in Figures (2) and (3) for spatial schemes with artificial dissipation and effective order of accuracy as given in the plot legend, it is clear that for the BDF1 scheme, not much difference exists among the spatial discretizations with the exception of the first-order accurate discretization. In other words, the BDF1 scheme itself drives the overall numerical dissipation. On the other hand, for the ESDIRK4 scheme, it is clear that the artificial dissipation term drives the overall numerical dissipation of the scheme. This is evidenced by the fact that schemes with overall effective orders four and five, for instance, which share a common artificial dissipation term, are visually coincident. It should also be noted that almost universally, higher-order spatial discretizations are less dissipative, especially at low wave numbers, when the higher-order ESDIRK4 time integrator is used.

Of course, the dissipation of the scheme is not the whole story: dispersion error, as measured by the phase error, i.e. how fast a wave travels relative to how fast it theoretically should be traveling, also plays a key role as a source of numerical inaccuracy. Figures (4) and (5) plot the phase error for the BDF1 and ESDIRK4 time discretizations for all the same spatial discretizations that were immediately previously discussed. As can be seen for the backward-Euler time-discretization, universally, higher-order central differences have lower phase error for all wave numbers. This trend becomes especially apparent when the overall order-of-accuracy discretizations are considered. These same observations are even more pronounced when the ESDIRK4 time discretization is considered in Figure (5).

Figure (6) plots the magnitude of the growth factor (6(a)) and the phase error (6(b)) for the six different implicit time integration schemes under consideration for the overall fifth-order accurate spatial discretization. In regards to
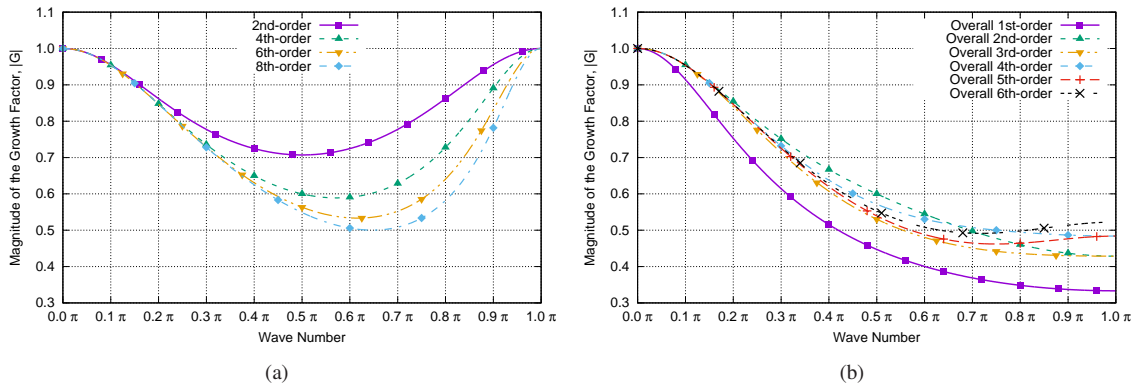
Figure 2: The magnitude of the growth factor for the first-order accurate backward-Euler time discretization at a *CFL* number of one (a) for second-, fourth-, sixth-, and eighth-order accurate central differences with no artificial dissipation and (b) for the combination of convection and artificial dissipation terms that produces first through sixth spatial orders of accuracy



Figure 3: The magnitude of the growth factor for the fourth-order accurate ESDIRK4 time discretization at a *CFL* number of one (a) for second-, fourth-, sixth-, and eighth-order accurate central differences with no artificial dissipation and (b) for the combination of convection and artificial dissipation terms that produces first through sixth spatial orders of accuracy
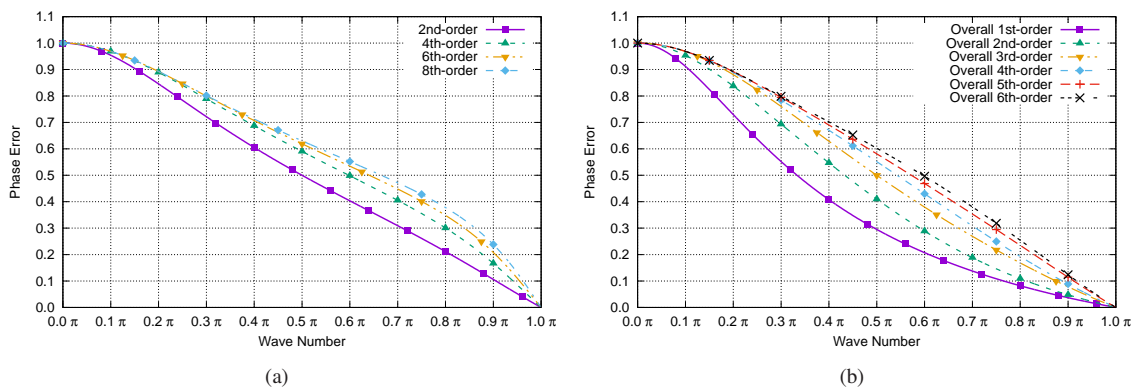


Figure 4: The phase error for the first-order accurate backward-Euler time discretization at a *CFL* number of one (a) for second-, fourth-, sixth-, and eighth-order accurate central differences with no artificial dissipation and (b) for the combination of convection and artificial dissipation terms that produces first through sixth spatial orders of accuracy
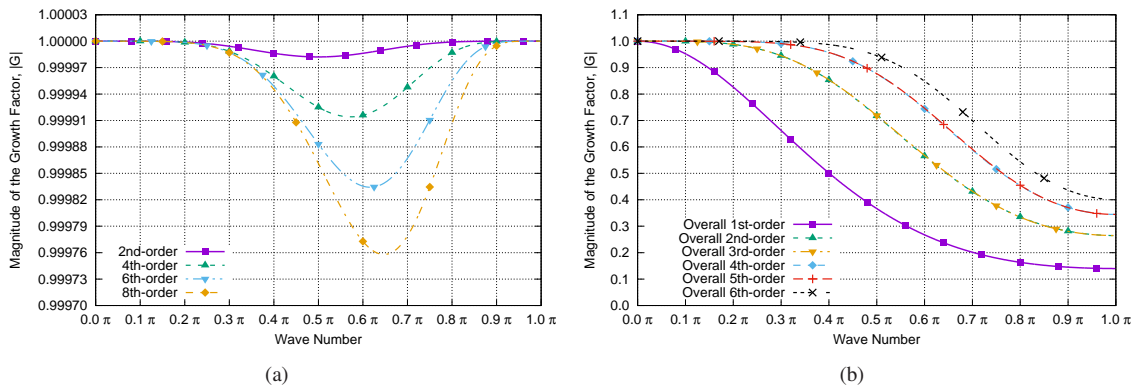
American Institute of Aeronautics and Astronautics

Figure 5: The phase error for the fourth-order accurate ESDIRK4 time discretization at a *CFL* number of one (a) for second-, fourth-, sixth-, and eighth-order accurate central differences with no artificial dissipation and (b) for the combination of convection and artificial dissipation terms that produces first through sixth spatial orders of accuracy
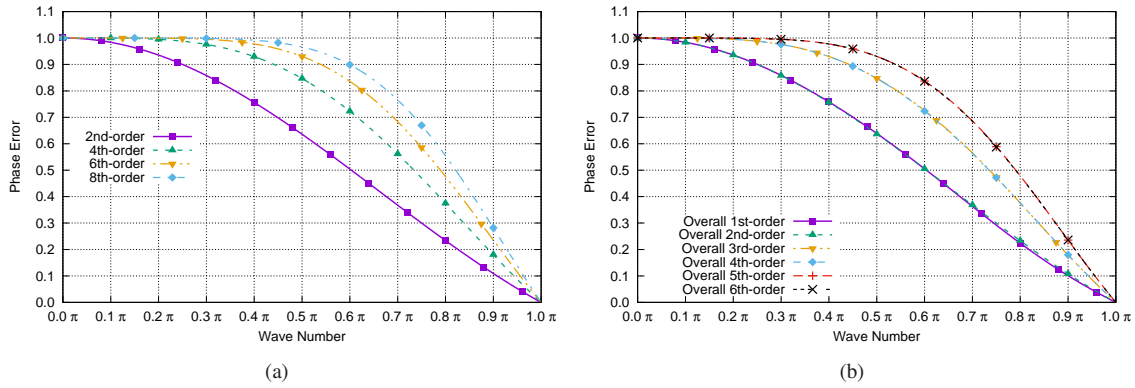
the growth factor, all of the ESDIRK schemes have very similar growth factor curves, especially in the lower half of the wave numbers. Crank-Nicolson is less dissipative than any of the three aforementioned schemes at all except the highest wave numbers, likely because of its small error constant, while backward-Euler is more dissipative at lower wave numbers and less dissipative at higher wave numbers, which is not a desirable arrangement. When it comes to phase error, generally, more accurate temporal discretizations have lower phase error, as can be seen from Figure (6(b)). This is true at all but the highest wave numbers. The exception to this trend is BDF1, which has the highest phase error of all the schemes at all wave numbers.
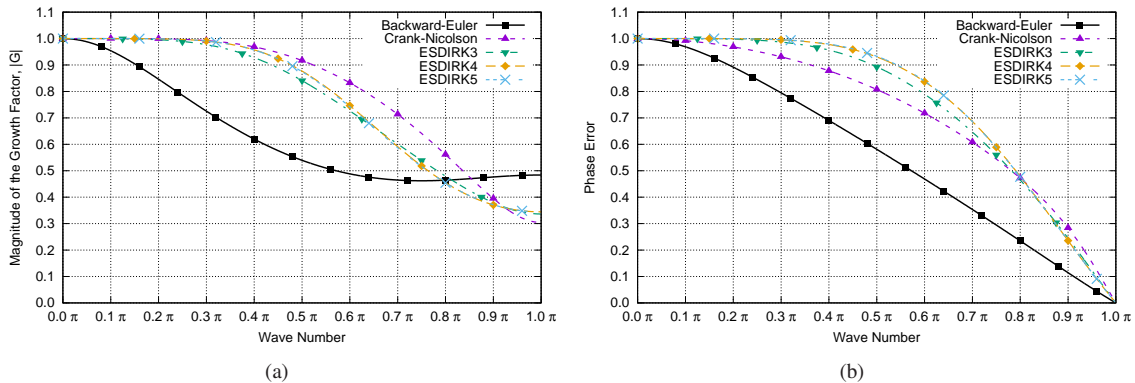


Figure 6: The (a) magnitude of the growth factor and (b) phase error for the time discretizations shown in the legend at a *CFL* number of one with overall effective fifth-order spatial accuracy

Figure (7) plots the dissipation (7(a)) and dispersion (7(b)) for the overall fifth-order accurate spatial discretization and all of the time integrators for a *CFL* number of ten. This higher *CFL* number is plotted to assess how the spatial/temporal schemes respond when different parts of a grid have different cell sizes (as may occur in the presence of boundary layers) and to ascertain the effect of using larger time steps if, for instance, on a grid that would produce the desired spatial resolution, the spatial error is still the dominant form of error. At increased *CFL* numbers, the schemes are much more differentiated, with Crank-Nicolson clearly being the least dissipative and ESDIRK5 clearly being the least dispersive. In light of the fact that ESDIRK4 has five implicit stages whereas ESDIRK5 has seven implicit stages, the potential gains of ESDIRK5 over ESDIRK4 do not necessarily justify the increased cost. Indeed in the flow results section, it will be shown that for the problems presented in this work, ESDIRK5 only shows worthwhile accuracy gains over ESDIRK4 at high *CFL* numbers or on very resolved meshes.

Overall, the von Neumann analysis has shown that when a high-order spatial discretization is used a high-order time discretization should also be used. Using one without the other appears to be an inefficient choice. It will be shown that this is especially true on more refined spatial meshes. This analysis also shows that dispersion and dissipation are
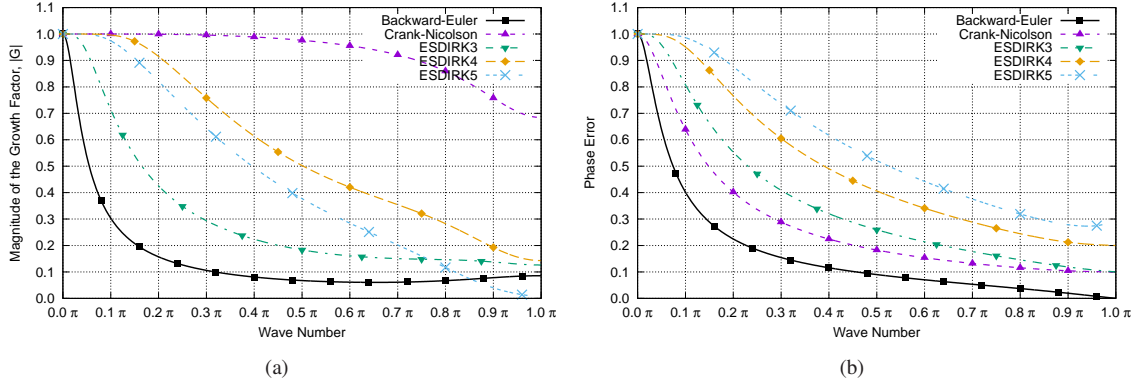
Figure 7: The (a) magnitude of the growth factor and (b) phase error for the time discretizations shown in the legend at a $CFL$ number of ten with overall effective fifth-order spatial accuracy

both important as sources of error. Indeed, it appears that dispersion error, in general, is the more important form of error since higher-order temporal schemes appear mostly to correspond to schemes with lower dispersion error but not necessarily lower dissipation error.

# IV.   Computational Results

Computational results are presented in the following subsections. First, one-dimensional solutions of the Euler equations are presented. Then, results of the three-dimensional convection of a two-dimensional (cylindrical) isentropic vortex are considered.

## A.   One-dimensional Results

The one-dimensional Euler equations serve as a simple test for the validation of the dissipation and dispersion characteristics derived in the von Neumann analysis. The periodic governing equations utilize conservative variables as expressed in equation (1), omitting the viscous and source terms. A Mach number $M_\infty = 0.5$ is chosen and the uniform background flow is defined by the following physical parameters:

$$\rho_\infty = 8.7077 \times 10^{-1} \frac{kg}{m^3}, \quad \rho u_\infty = 1.7458 \times 10^2 \frac{kg}{m^2 \cdot s}, \quad T_\infty = 400K, \quad R_\infty = 2.871 \times 10^2 \frac{J}{kg \cdot K}, \quad \gamma = 1.4 \qquad (20)$$

While the Euler equations are solved in divergence form, the von Neumann analysis assumes linearity, which can be accommodated by inducing only small perturbations with magnitude merely one-percent of the mean flow. The flow is perturbed in a physically consistent manner by introducing the perturbations using the characteristic variables. In this way, only the chosen wave numbers $\theta = k\Delta x$ can be excited. This process is given by the following equations:

$$Q_o \;=\; Q_\infty + M\delta\hat{Q}_{u,u\pm c} \qquad (21)$$
$$\delta\hat{Q}_{u,u\pm c} \;=\; \hat{\delta} \cdot \cos(kx) \qquad (22)$$

where $\hat{\delta} = 0.01$ or one percent of the quiescent flow value, as stated above. The subsequent evolution of the perturbation wave by the numerical scheme is then tracked in characteristic variable space, so that it can be directly compared to the dissipation and dispersion results supplied by the von Neumann analysis.

Only a single wavelength $L$ of the perturbation is contained in the domain. This wavelength and therefore the corresponding domain length is set to one meter. Resolutions $I$ of ten and twenty points per wave are used so it can be seen that there are necessarily only ten and twenty points, respectively, in the domain. These resolutions correspond to a wave numbers of $\theta = 0.2\pi$ and $\theta = 0.1\pi$, respectively. Cumulative dissipation $|G|_{cum}$ and dispersion error $\phi_{e,cum}$ after a number of time steps $N$ time steps can be predicted from the von Neumann analysis, as given by the following equations (23):

$$\begin{aligned} |G|_{cum} &\;=\; |G|_{u+c}^N \\ \phi_{e,cum} = \frac{\Delta x_{cum}}{L} &\;=\; \frac{N \cdot CFL_{u+c}}{I \cdot L}(1 - \phi_e) \end{aligned} \qquad (23)$$

American Institute of Aeronautics and Astronautics

where $\Delta x_{cum}$ is the cumulative absolute distance the wave is out of phase. Thus, $\phi_{e,cum}$ is expressed as the fraction of the wavelength for which the solution is out of phase. The following computational cases focus on the right running acoustic wave ($\hat{q}_{u+c}$) and are compared to theoretical results from von Neumann analysis.

Table (1) and Figure (8) compare the performance of Crank-Nicolson and the three ESDIRK schemes using an overall fifth-order accurate spatial discretization with artificial dissipation. There are ten points per wave, a *CFL* number of unity is used, and the wave is advanced one period. As can be seen, all schemes exhibit low dissipation, while Crank-Nicolson exhibits noticeable dispersion. Examining the error plot, it becomes clear that the higher the order of the scheme, the lower error it exhibits, with very little difference apparent between ESDIRK4 and ESDIRK5. The following pattern should also be observed and noted: when the error is primarily dispersive, the minimum error will occur at a position near the extrema of the waveform; however, when the error is primarily dissipative, the minimum error will occur at a position near the inflection points of the waveform.

Table 1: Von Neumann and numerical results for the forward moving acoustic wave for the Euler equations with artificial dissipation, with ten points per wave, at a *CFL* number of one, after one period of convection

| Scheme | Dissipation Error | | Dispersion Error | |
|---|---|---|---|---|
| | VNA | Simulation | VNA | Simulation |
| CN | $8.42 \times 10^{-3}$ | $2.77 \times 10^{-2}$ | $3.14 \times 10^{-2}$ | $3.08 \times 10^{-2}$ |
| ESDIRK3 | $4.25 \times 10^{-2}$ | $4.26 \times 10^{-2}$ | $2.47 \times 10^{-3}$ | $2.39 \times 10^{-2}$ |
| ESDIRK4 | $9.25 \times 10^{-3}$ | $9.26 \times 10^{-3}$ | $5.37 \times 10^{-4}$ | $5.26 \times 10^{-4}$ |
| ESDIRK5 | $9.31 \times 10^{-3}$ | $9.31 \times 10^{-3}$ | $4.10 \times 10^{-4}$ | $4.00 \times 10^{-4}$ |



(a)                                (b)

Figure 8: (a) Amplitude and (b) error in the convection of the forward moving acoustic wave for the Euler equations including artificial dissipation, with ten points per wave, at a *CFL* number of one, after one period of convection

Table (2) and Figure (9) shows the same data as previously for the same *CFL* number and resolution, but after ten periods of convection. As is clearly seen, error accumulates as solution time increases, with Crank-Nicolson exhibiting much more dispersion error and ESDIRK3 showing much more dissipation error. ESDIRK4 and ESDIRK5 even show a small amount of dissipation, but the differences between them are still mostly unnoticeable.

Table 2: Von Neumann and numerical results for the forward moving acoustic wave for the Euler equations with artificial dissipation, with ten points per wave, at a *CFL* number of one, after ten periods of convection

| Scheme | Dissipation Error | | Dispersion Error | |
|---|---|---|---|---|
| | VNA | Simulation | VNA | Simulation |
| CN | $8.11 \times 10^{-2}$ | $8.49 \times 10^{-2}$ | $3.14 \times 10^{-1}$ | $3.14 \times 10^{-1}$ |
| ESDIRK3 | $3.52 \times 10^{-1}$ | $3.60 \times 10^{-1}$ | $2.47 \times 10^{-2}$ | $2.41 \times 10^{-2}$ |
| ESDIRK4 | $8.88 \times 10^{-2}$ | $8.93 \times 10^{-1}$ | $5.37 \times 10^{-3}$ | $5.22 \times 10^{-3}$ |
| ESDIRK5 | $8.93 \times 10^{-2}$ | $8.96 \times 10^{-2}$ | $4.10 \times 10^{-3}$ | $4.00 \times 10^{-3}$ |

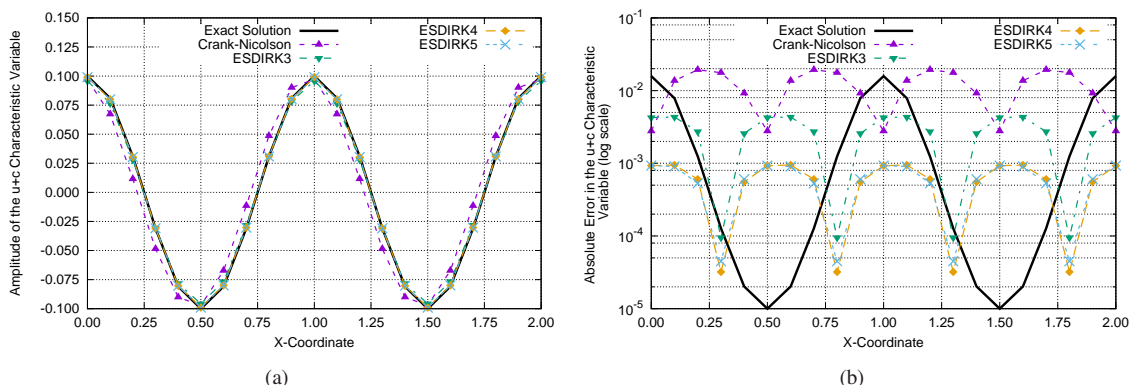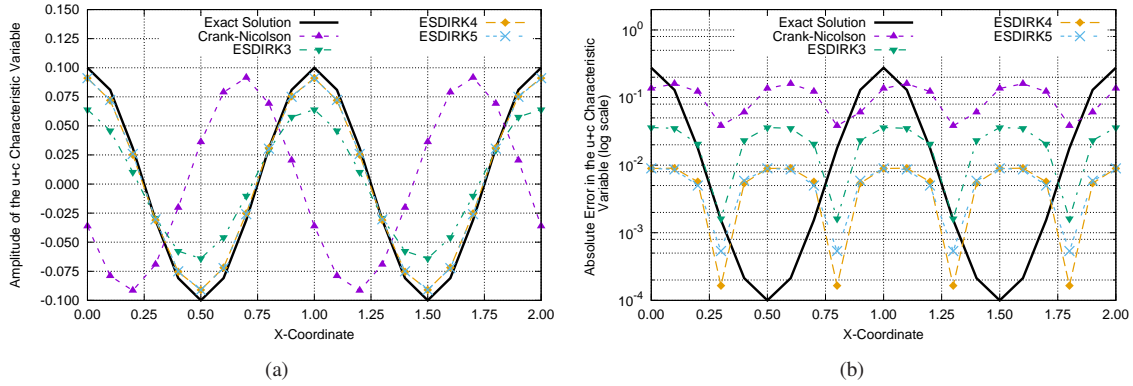American Institute of Aeronautics and Astronautics

(a)



(b)

Figure 9: (a) Amplitude and (b) error in the convection of the forward moving acoustic wave for the Euler equations including artificial dissipation, with ten points per wave, at a $CFL$ number of one, after ten periods of convection

For all of the remaining one-dimensional cases, resolution has been increased to twenty points per wave. Table (3) and Figure (10) chart a case with the same $CFL$ number of one and ten periods of progression, as previously, but at this increased spatial resolution. The dispersive properties of Crank-Nicolson are still evident at this finer resolution, but the dissipation of ESDIRK3 appears to have been mostly eliminated. On examination of the error subplot, it becomes clear ESDIRK3 still exhibits much higher dissipation than either ESDIRK4 or ESDIRK5.

Table 3: Von Neumann and numerical results for the forward moving acoustic wave for the Euler equations with artificial dissipation, with twenty points per wave, at a $CFL$ number of one, after ten periods of convection

| Scheme | Dissipation Error | | Dispersion Error | |
|---|---|---|---|---|
| | VNA | Simulation | VNA | Simulation |
| CN | $3.05 \times 10^{-3}$ | $1.00 \times 10^{-2}$ | $8.11 \times 10^{-2}$ | $8.11 \times 10^{-2}$ |
| ESDIRK3 | $5.02 \times 10^{-2}$ | $5.02 \times 10^{-1}$ | $1.51 \times 10^{-3}$ | $1.53 \times 10^{-3}$ |
| ESDIRK4 | $3.13 \times 10^{-3}$ | $3.13 \times 10^{-3}$ | $1.50 \times 10^{-4}$ | $1.58 \times 10^{-4}$ |
| ESDIRK5 | $3.14 \times 10^{-3}$ | $3.14 \times 10^{-3}$ | $6.78 \times 10^{-5}$ | $6.90 \times 10^{-5}$ |

Implicit time integration methods, like the ones presented herein, are unconditionally stable and as such can be run at higher $CFL$ numbers than stability considerations would allow for explicit schemes. Increased $CFL$ numbers result in larger time steps, which increases the amount of temporal error. If the solution is already in a regime where spatial error dominates, an increased $CFL$ number will not greatly affect the overall error; however, if temporal error is dominant, the overall accuracy of the solution will be degraded. Results for simulations at $CFL_{u+c} = 10$ and which are advanced for only two time steps, corresponding to one solution period, are shown in Table (4) and Figure (11). In this figure, the differences in the accuracy among the various temporal schemes under consideration are clear. As the von Neumann analysis predicted, Crank Nicolson preserves amplitude well yet is too dispersive, with its solution lagging about 36% of the wavelength. ESDIRK3 exhibits high dissipation and dispersion, damping 50% of the amplitude and lagging the exact solution by 20% of the wavelength. ESDIRK4 and ESDIRK5 are still very well behaved with the solutions using them showing 99% and 95% of the original amplitude and phase errors of only about 5% and 1% of the wavelength, respectively). However, the superior precision of ESDIRK5 is evident for this case; supporting the predictions of von Neumann analysis, the computational results show that the fourth-order ESDIRK scheme is less dissipative yet more dispersive than the fifth-order scheme.

Finally, Table (5) and Figure (12) performance of the temporal schemes under consideration for a very long solution time. In fact, each wave is advanced for twenty-thousand time steps at a $CFL_{u+c} = 1$, meaning that the wave convects for one-thousand wave lengths. The popular Crank-Nicolson scheme does well to preserve the magnitude of the wave, which has 74% of its original amplitude at the end of the computation. However, the Crank-Nicolson solution suffers tremendously from dispersion error. To best capture the wave features, the aforementioned figure features only two wavelengths, which obscures the fact that the Crank-Nicolson solution is actually about eight wavelengths behind its correct position. As the plot shows, ESDIRK3 is obviously extremely dissipative and effectively damps
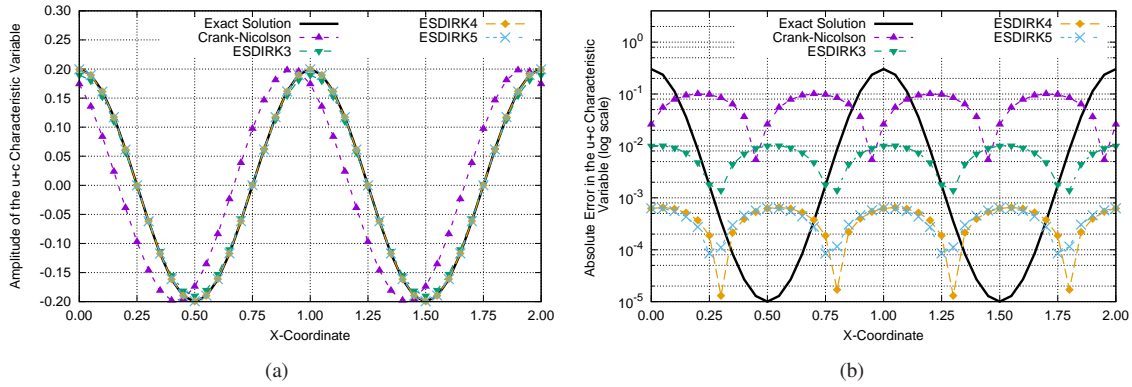
(a)                                          (b)

Figure 10: (a) Amplitude and (b) error in the convection of the forward moving acoustic wave for the Euler equations including artificial dissipation, with twenty points per wave, at a $CFL$ number of one, after ten periods of convection

Table 4: Von Neumann and numerical results for the forward moving acoustic wave for the Euler equations with artificial dissipation, with twenty points per wave, at a $CFL$ number of ten, after one period of convection

| | **Dissipation Error** | | **Dispersion Error** | |
|---|---|---|---|---|
| **Scheme** | VNA | Simulation | VNA | Simulation |
| Crank-Nicolson | $0.01 \times 10^{-1}$ | $0.02 \times 10^{-1}$ | $3.61 \times 10^{-1}$ | $3.50 \times 10^{-1}$ |
| ESDIRK3 | $4.90 \times 10^{-1}$ | $4.90 \times 10^{-1}$ | $1.92 \times 10^{-1}$ | $2.00 \times 10^{-1}$ |
| ESDIRK4 | $0.07 \times 10^{-1}$ | $0.07 \times 10^{-1}$ | $4.90 \times 10^{-2}$ | $5.00 \times 10^{-2}$ |
| ESDIRK5 | $0.51 \times 10^{-1}$ | $0.55 \times 10^{-1}$ | $1.39 \times 10^{-2}$ | $1.00 \times 10^{-2}$ |



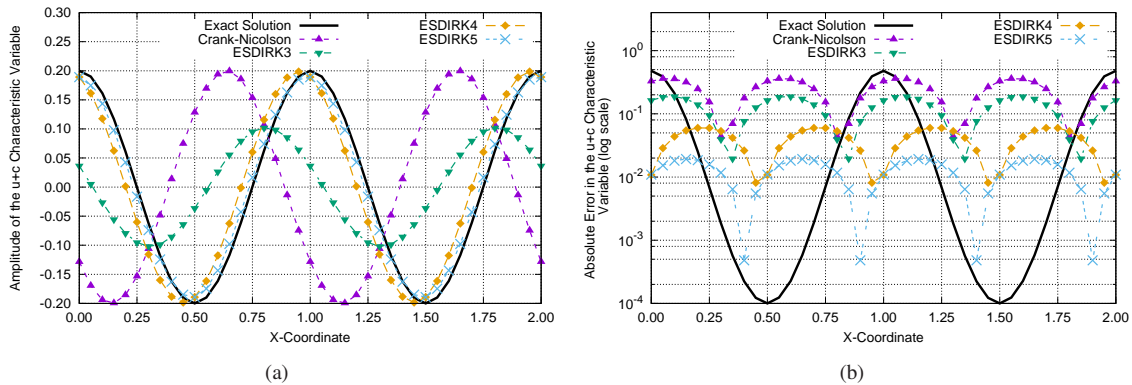(a)                                          (b)

Figure 11: (a) Amplitude and (b) error in the convection of the forward moving acoustic wave for the Euler equations including artificial dissipation, with twenty points per wave, at a $CFL$ number of ten, after one period of convection

American Institute of Aeronautics and Astronautics

the perturbation entirely. ESDIRK4 and ESDIRK5, on the other hand, exhibit excellent dissipation and dispersion characteristics, especially given the long solution time. For both schemes, damping is kept to approximately 27% as the final solution maintains about 73% of the the correct amplitude. Dispersion is $\approx$ 3% of the wavelength. The ability of ESDIRK4 and ESDIRK5 to preserve amplitude and phase in the presence of artificial dissipation seems highly attractive for time-accurate solutions with high-order spatial discretizations. Figure(12(b)) shows the exact solution along with the absolute error of ESDIRK4 and ESDIRK5 schemes, capturing the combined effect of cumulative dissipation and dispersion errors and highlighting that ESDIRK5 does, in fact, have slightly lower overall error than ESDIRK4.

Table 5: Von Neumann and numerical results for the forward moving acoustic wave for the Euler equations with artificial dissipation, with twenty points per wave, at a $CFL$ number of one, after one-thousand periods of convection

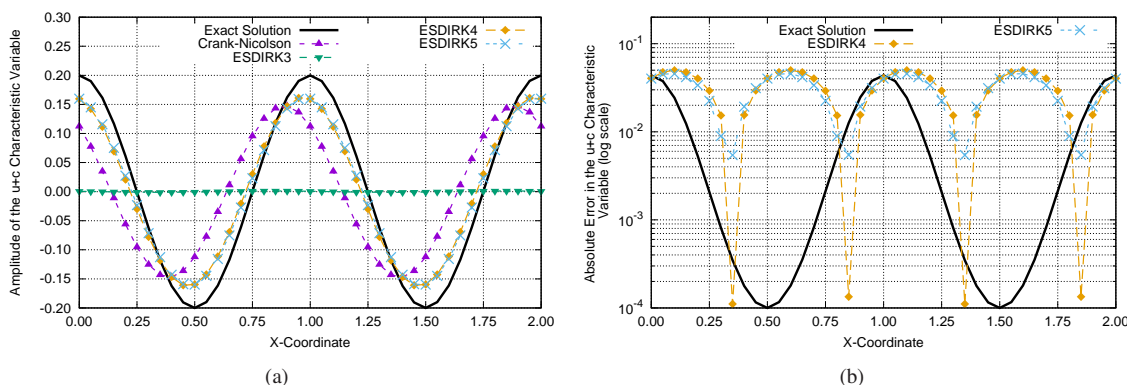| Scheme | Dissipation Error | | Dispersion Error | |
|---|---|---|---|---|
| | VNA | Simulation | VNA | Simulation |
| CN | $2.63 \times 10^{-1}$ | $2.65 \times 10^{-1}$ | $8.11 \times 10^{0}$ | $8.10 \times 10^{0}$ |
| ESDIRK3 | $9.94 \times 10^{-1}$ | $9.94 \times 10^{-1}$ | $1.51 \times 10^{-1}$ | $1.00 \times 10^{-1}$ |
| ESDIRK4 | $2.69 \times 10^{-1}$ | $1.95 \times 10^{-1}$ | $1.50 \times 10^{-2}$ | $3.00 \times 10^{-2}$ |
| ESDIRK5 | $2.70 \times 10^{-1}$ | $2.01 \times 10^{-1}$ | $6.78 \times 10^{-3}$ | $2.50 \times 10^{-2}$ |



Figure 12: (a) Amplitude and (b) error in the convection of the forward moving acoustic wave for the Euler equations including artificial dissipation, with twenty points per wave, at a $CFL$ number of one, after one-thousand periods of convection

These one-dimensional Euler computations serve as a validation of the von Neumann analysis results and have helped inform perceptions of the strengths and weaknesses of the temporal schemes considered herein. Having established expected performance near the linear regime of the Euler equations, the next section presents a more complex, three-dimensional case.

## B. Convection of an Isentropic Vortex

The isentropic vortex is a generally localized set of specific perturbations, which occur across a broad range of wave numbers, to an otherwise uniform flow. The perturbations occur in the $x$- and $y$-velocity components and the temperature. Because these perturbations are isentropic, they result in perturbations in the pressure, density, and energy of the flow as well. The velocity and temperature perturbations of the isentropic vortex are as follows:

$$\delta u = -\sqrt{R_\infty T_\infty} \frac{\alpha}{2\pi} (y - y_0) e^{\phi(1-r^2)} \tag{24}$$

$$\delta v = \sqrt{R_\infty T_\infty} \frac{\alpha}{2\pi} (x - x_0) e^{\phi(1-r^2)} \tag{25}$$

$$\delta T = T_\infty \frac{\alpha^2 (\gamma - 1)}{16\phi\gamma\pi^2} e^{2\phi(1-r^2)} \tag{26}$$

where $\alpha$ determines the strength of the vortex and $\phi$ determines the gradient of the vortex, which in turn determines vortex size. Higher values of $\phi$ correspond to smaller vortices with more rapidly changing temperature and velocity from the edge to the center. The vortex center is at $(x_0, y_0)$ with the distance to this center from a coordinate $(x, y)$ given as $r = \sqrt{(x - x_0)^2 + (y - y_0)^2}$. If these perturbations look a little different from those in other publications, it is because they are in dimensional form. Many other publications assume a particular non-dimensionalization, but do not always explicitly state that fact.[4]

For all of the vortex test cases presented herein $\alpha = 4$ and $\phi = 1$; as a result, the vortex has a diameter of about $2.2m$ (vortex diameter is determined as the diameter of the area where the density perturbation is more than five-percent of the free stream value). The cases are run at a free stream Mach number of $M_\infty = 0.5$ in the x-direction. The free stream density is set to be $\rho_\infty = 1.0 \frac{kg}{m^3}$. It was desired that the free stream speed of sound be a round number close to its typical value for air, so $c_\infty = 400 \frac{m}{s}$ was chosen. Given that $R_\infty = 287.11 \frac{J}{kg \cdot K}$ and $\gamma = 1.4$ for air, this necessarily means that free stream temperature and pressure have the following values $T_\infty = 398.06K$ and $p_\infty = 114285.7Pa$. Thus, the free stream conserved variables have the following values:

$$\rho_\infty = 1.0 \frac{kg}{m^3}, \quad \rho u_\infty = 200.0 \frac{kg}{m^2 \cdot s}, \quad \rho v_\infty = 0.0 \frac{kg}{m^2 \cdot s}, \quad \rho w_\infty = 0.0 \frac{kg}{m^2 \cdot s}, \quad \rho e_{0,\infty} = 305714.3 \frac{kg}{m \cdot s^2} \tag{27}$$

Given the strength of the vortex and the free stream Mach number, this test case will clearly be affected by the non-linearity of the Euler equations

First, the formal orders of accuracy of both the spatial and temporal discretizations examined herein are establishes by convecting the isentropic vortex, described above, for a short amount of time. For spatial accuracy, the vortex is convected for one time step whose fixed length is $\Delta t = 0.0000107421875s$ on a computational mesh that is $22.0m \times 22.0m$ in the x- and y-directions and whose resolution varies. Because the flow should have no variation in the z-direction, four points were used in that dimension for all grid resolutions. As a result, the length of the grid in $z$ varies depending on the $x$ and $y$ grid resolution such that $\Delta x = \Delta y = \Delta z$. Thus, for a grid resolution of one-hundred nodes in the x- and y-directions, the mesh would be $0.88m$ in the z-direction. Boundaries are periodic in all three directions. The given time-step size corresponds to a $CFL$ number close to one when the mesh resolution is 1600 points in each of the x- and y-directions. Figure (13) plots the results of the spatial-order-of-accuracy tests. As can be seen, the errors of all the spatial schemes considered exhibit the expected convergence trends as resolution increases. Since both axes are given in terms of powers of two in Figure (13), a third-order scheme, for example, is expected to decrease three grid lines for every one grid line decrease in $dx$.



Figure 13: Variation of the $L_2$-norm of solution error in density with spatial resolution for the isentropic vortex after one time step, demonstrating formal order-of-accuracy convergence for the given spatial schemes

For the temporal accuracy study the vortex is convected for $0.0064s$ on a computational mesh that is $24.0m \times 24.0m \times 0.04m$ with a fixed resolution of $2400 \times 2400 \times 4$ nodes in each of the three directions, yielding $\Delta x = \Delta y =$

American Institute of Aeronautics and Astronautics

$\Delta z = 0.01$. Again, boundaries are periodic in all three dimensions. This case is run with different time step sizes ranging from as large as $0.0064s$ to as small as $6.25 \times 10^{-6}s$ with each smaller time step being $\frac{1}{2}$ as large as its immediately bigger time step. These time steps correspond to $CFL$ numbers ranging from 896 to 0.875. Obviously, this means that for smaller time-step sizes, the solution must be run for a greater number of time steps to achieve the overall $0.0064s$ of solution time. Figure (14) plots the density error convergence of Crank-Nicolson as well as third-, fourth-, and fifth-order ESDIRK. As can be seen, all four schemes demonstrate the expected order-of-accuracy error convergence.
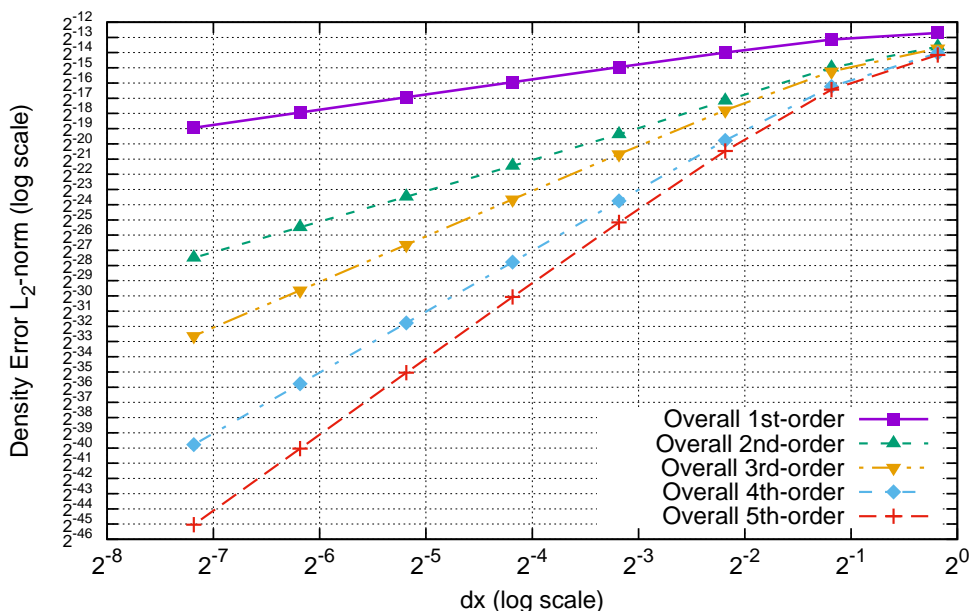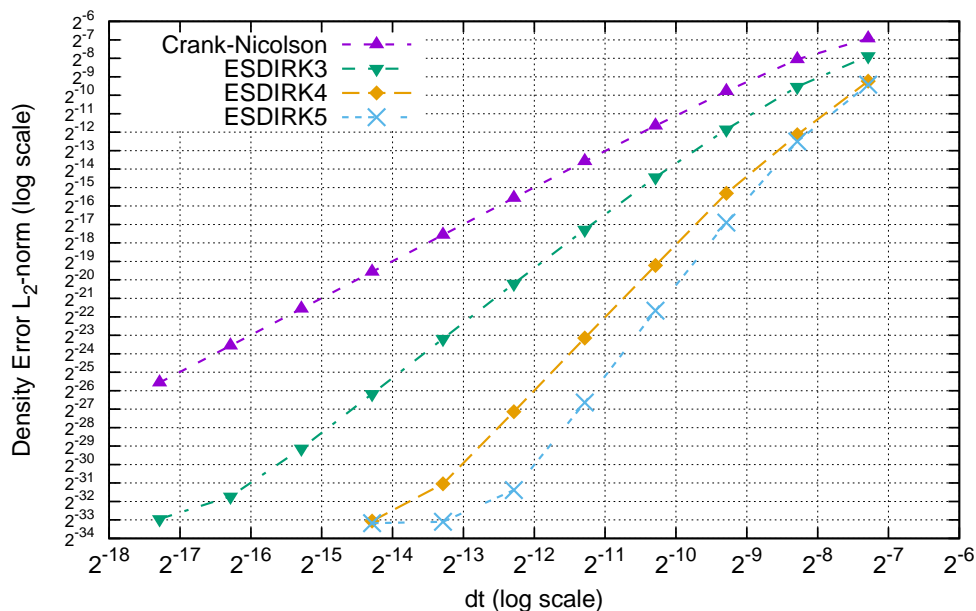


Figure 14: Variation of the $L_2$-norm of solution error in density with time-step size for the isentropic vortex after 0.0064 seconds, demonstrating formal order-of-accuracy convergence for the given temporal schemes

Next, the vortex with conditions as given above, is convected for a much longer time on the same mesh that was used for the spatial-accuracy study, i.e. $22.0m \times 22.0m$ in the $x$- and $y$-directions. Since, as was stated earlier, the vortex diameter is about $2.2m$, the domain is about ten vortex diameters long and there are eleven points across the vortex on a mesh with one-hundred nodes in $x$ and $y$. The density perturbation of the vortex along its x-direction center-line after two and four domain lengths of convection using the stated grid, at a free stream $CFL$ number of about one (1.09375 to be precise), and for the four different time discretizations is shown in Figure (15). As can be seen, all three ESDIRK schemes produce the same results while Crank-Nicolson shows only a small variation, even after forty vortex widths of convection. This results seems to indicate that for this mesh at a $CFL$ number of one, spatial error dominates temporal error for all time schemes under consideration.

To verify the spatial-error-dominance hypothesis, Figure (16(a)) plots solution error after a short time ($0.0275s$) versus grid resolution at a constant $CFL$ number of about one. Because the $CFL$ number is held constant, the temporal resolution necessarily increases at the same rate as the spatial resolution from right to left along the $x$-axis of the chart. As can be seen, all three ESDIRK schemes as well as the explicit third-order Runge-Kutta-Wray, which is frequently used as the time-integrator in high-order Cartesian codes and is included for the sake of comparison, have fifth-order error convergence. Crank-Nicolson initially shows fifth-order error convergence, but its accuracy reduces to second-order as resolution increases, signaling that at higher resolution, the temporal scheme becomes the dominant source of error. It should be noted that the one-hundred node grid used above corresponds to the second point from the right (as noted), meaning it is clearly in the spatially-dominant regime for all time schemes. Figure (16(b)) shows the error of the different time schemes relative to the the ESDIRK5 scheme at a $CFL$ number of about one (to allow for more straightforward visualization of the differences). As can be seen, at finer resolutions, ESDIRK3 has about half the error of RK-Wray, while ESDIRK4 and ESDIRK5 have the same amount of error for the entire domain of the plot, signaling that spatial error is clearly dominant for these time schemes at all tested grid resolutions.

Referring again to Figure (16), it can be seen that Crank-Nicolson starts to have a different slope at the third point from the left, which corresponds to forty-one points across the vortex, or four times the resolution shown previously.

Figure 15: Density at the vortex center line for the time discretization given in the legend with eleven points across the vortex at a $CFL$ number close to one after convecting (a) two periods, (b) four periods .
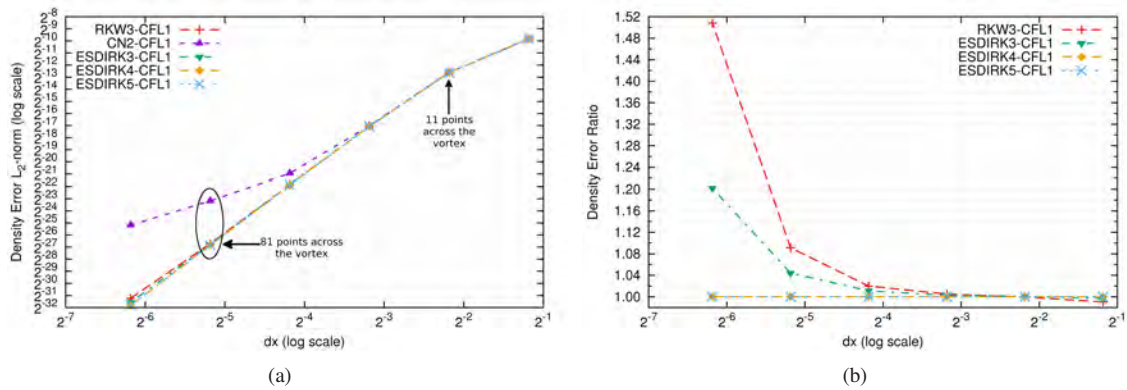


Figure 16: Comparison of the density error for different time discretizations at a $CFL$ number of one for (a) absolute error and (b) error scaled by the ESDIRK5 error at a $CFL$ number close to one.

A significant difference in error, however, is not seen until the next point to the left with eighty-one points across the vortex. Figure (17) shows the density at the vortex center line for the vortex on this eight-times resolution grid after four periods of convection. All lines appear to overlay the exact solution in the (a) subplot. The (b) subplot, therefore, displays the absolute error, i.e. the absolute value of the difference between the numerical and exact solutions. It can clearly be seen in this figure that Crank-Nicolson has about an order and a half higher error than the three ESDIRK schemes, which themselves have quite similar error curves. This is the expected result taking into account the trends seen in the previous figure.



Figure 17: (a) Density and (b) absolute error in density at the vortex center line for the time discretization given in the legend with eighty-one points across the vortex at a $CFL$ number of about one after convecting four periods.

Figure (18) shows the density profile at the center-line for the isentropic vortex at a $CFL$ number of about eight on a grid with one-hundred points in the $x$- and $y$-directions after having convected for two and four domain lengths. An additional curve has been added to these plots, designated "CN2-MAX" corresponding to the profile at the maximum density perturbation for the Crank-Nicolson time scheme. This additional curve was added because the vortex has meandered off the center-line by six grid spacings after two domain lengths and by ten grid spacings after four domain lengths of travel. As can be seen, differences among all schemes besides ESDIRK4 and ESDIRK5 are apparent at this larger $CFL$ number. Additionally, it can be observed that, although Crank-Nicolson does an excellent job at preserving the magnitude of the perturbation (low dissipation), the fact that, because of dispersion error, the vortex travels along an incorrect path (it convects both faster and at a slightly downward angle compared to how it should convect), actually leads to this scheme's having higher error than the more dissipative, but less dispersive ESDIRK3 scheme.
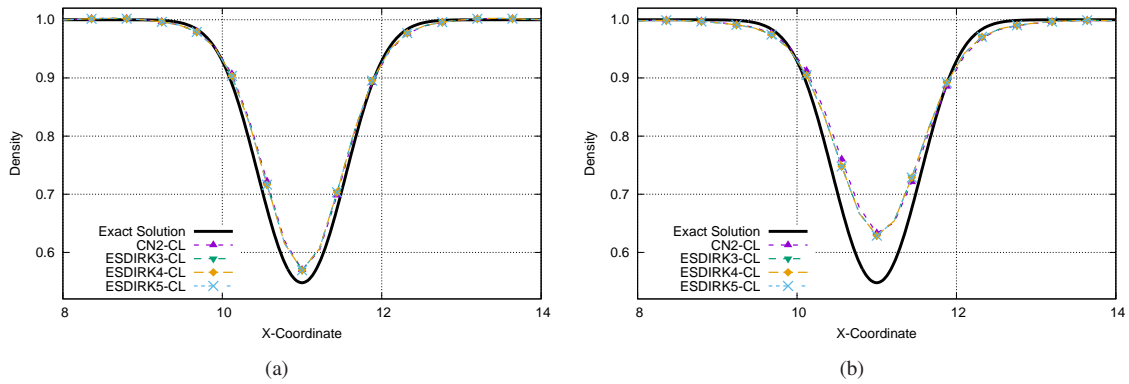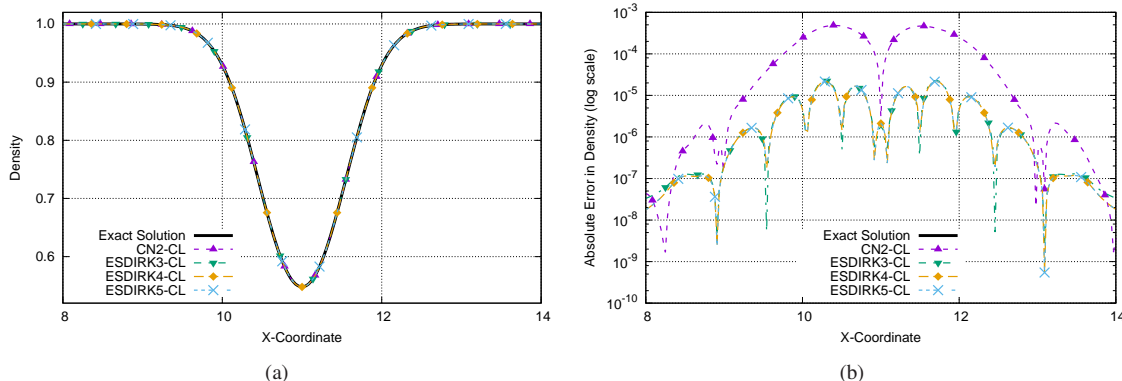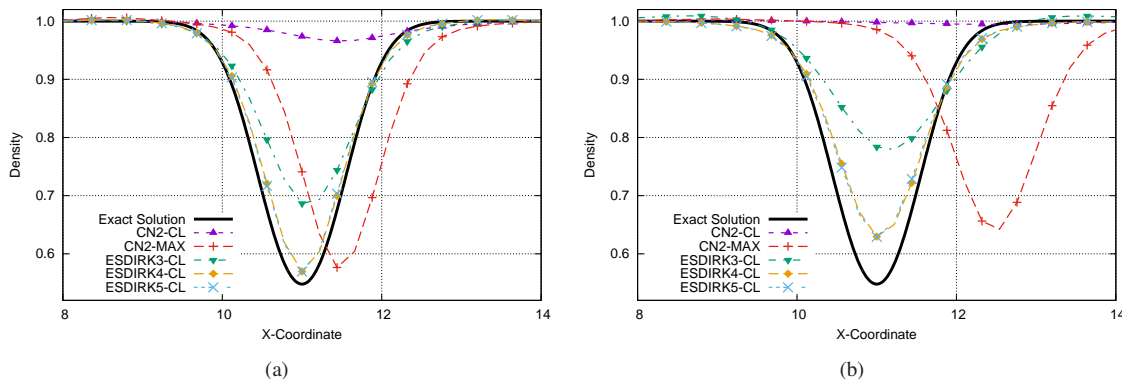


Figure 18: Density at the vortex center line for the time discretization given in the legend with eleven points across the vortex at a $CFL$ number of about eight after convecting (a) two periods and (b) four periods.

Finally, Figure (19) is analogous to Figure (16), plotting temporal scheme error at a constant $CFL$ number of about eight versus temporal and spatial resolution for the three ESDIRK schemes. As can be seen from the (a) subfigure, ESDIRK3 converges as third order for all resolutions, having much higher error at fine resolutions. As such, its error dwarfs the error of the other two ESDIRK schemes; thus, it was not included in subfigure (b). The second plot

demonstrates that for ESDIRK5, error is roughly independent of resolution, while relative error increases at better resolutions when the ESDIRK4 scheme is used. This is the expected result and points toward a preference of having the order of accuracy of the selected time scheme be the same as that of the selected spatial scheme to guarantee that overall error always converges at a constant slope.



(a)

(b)

Figure 19: Comparison of the density error for ESDIRK4 and ESDIRK5 time discretizations and a *CFL* number of about eight for (a) absolute error and (b) error scaled by the ESDIRK5 error at a *CFL* number close to one.
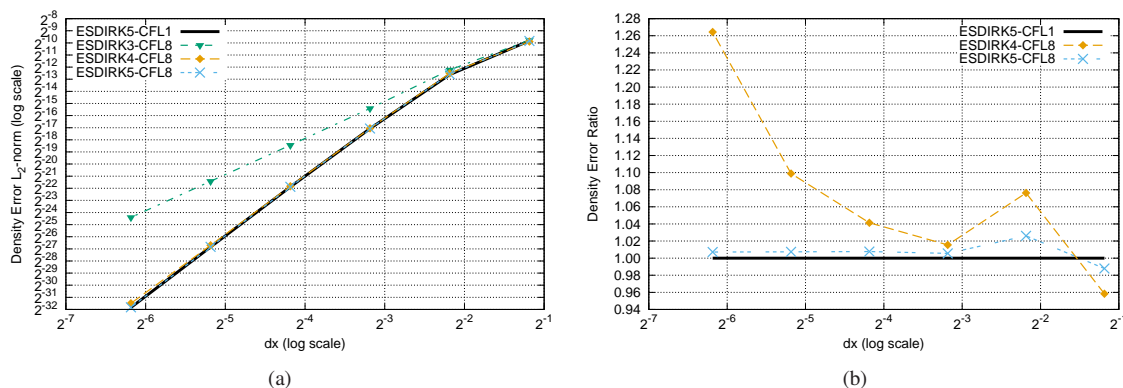
# V.  Conclusions and Future Work

The von Neumann analysis presented herein highlights advantages and disadvantages of the various time integrators. As expected, Crank-Nicolson, with its low error constant (the lowest of all second-order *A*-stable linear multistep methods),[3] performs well in terms of dissipation error, but is more dispersive because of its second-order accuracy. Moreover, its lack of *L*-stability, as is frequently cited,[4] remains a concern. As such, the six-stage (utilizing five implicit stages that require solution) ESDIRK4 appears to strike the best compromise between diffusion and dispersion errors, while its stage-count makes it a candidate, in terms of efficiency, for the preferred scheme. The compromise nature of this choice becomes especially apparent at *CFL* numbers greater than one.

The computational results tend to support the choice of ESDIRK4 as the preferred temporal integrator for fifth-order spatial schemes. It performs just as well as ESDIRK5 for typical time-step sizes and mesh resolutions. That being said, having the order of accuracy of the spatial and temporal schemes being the same does have the advantage of guaranteeing that the ratio of spatial to temporal error remains constant no matter the grid resolution at a given, constant *CFL* number.

This work clearly demonstrates that the common practice of using a third-order time integrator (like Runge-Kutta-Wray) coupled with a fifth-order spatial discretization is inadequate. As the grid is refined, the time step must be refined to a greater degree to experience an overall fifth order accurate decrease in the overall error. Specifically, if spatial resolution is doubled, spatial error will theoretically decrease by a factor of thirty-two while temporal error would only decrease by a factor of eight if the *CFL* number were kept constant. To get the same factor of thirty-two decrease temporal resolution would need to increase by a factor of $2^{5/3} \approx 3.175$.

Future work should be divided into three areas. First, *L*-stable Runge-Kutta time integrators whose growth factors decrease more slowly away from the origin in the complex left half of the eigenvalue plane should be developed for use with high-Reynolds number flows. Schemes with these properties (if they exist) should prove to have lower dissipation error while retaining the dispersion error characteristics of high-order temporal schemes already observed. Additionally, the present work highlights the need for lower error spatial schemes with the same formal order of accuracy. Such spatial discretizations would take maximum advantage of the high-order time discretizations both on coarser meshes and when using *CFL* numbers around one. Candidates for lower-error spatial schemes include compact-difference schemes[16] for their enhanced spatial resolution and filtering schemes[17, 18] because of their potential for highly scale-discriminant damping. Finally, a third area for future work is to add the preconditioning techniques described above[8] to the current methods. By adding preconditioning, more efficient and accurate solutions should be produced.

# A.   Butcher Tableaux

This appendix presents the Butcher Tableaux for all the of the Runge-Kutta schemes presented herein. The tableaux for the non-ESDIRK schemes can be referenced in Butcher[19] while the tableaux for the ESDIRK schemes are credited to these sources.[1,2]

$$\begin{array}{c|c} 1 & 1 \\ \hline & 1 \end{array}$$

**Implicit, First-order**
**Backward-Euler**

$$\begin{array}{c|cc} 0 & 0 & 0 \\ 1 & 1/2 & 1/2 \\ \hline & 1/2 & 1/2 \end{array}$$

**Implicit, Second-order**
**Crank-Nicolson**

$$\begin{array}{c|ccc} 0 & 0 & 0 & 0 \\ 8/15 & 8/15 & 0 & 0 \\ 2/3 & 1/4 & 5/12 & 0 \\ \hline & 1/4 & 0 & 3/4 \end{array}$$

**Explicit, Third-order**
**Runge-Kutta-Wray**

$$\begin{array}{c|cccc} 0 & 0 & 0 & 0 & 0 \\ 1/4 & 1/4 & 0 & 0 & 0 \\ 1/3 & 0 & 1/3 & 0 & 0 \\ 1/2 & 0 & 0 & 1/2 & 0 \\ \hline & 0 & 0 & 0 & 1 \end{array}$$

**Explicit, Fourth-order**
**Jameson-Runge-Kutta**

$$\begin{array}{c|cccc}
0 & 0 & 0 & 0 & 0 \\[4pt]
\frac{1767732205903}{2027836641118} & \frac{1767732205903}{4055673282236} & \frac{1767732205903}{4055673282236} & 0 & 0 \\[4pt]
\frac{3}{5} & \frac{2746238789719}{10658868560708} & -\frac{640167445237}{6845629431997} & \frac{1767732205903}{4055673282236} & 0 \\[4pt]
1 & \frac{1471266399579}{7840856788654} & -\frac{4482444167858}{7529755066697} & \frac{11266239266428}{11593286722821} & \frac{1767732205903}{4055673282236} \\[4pt]
\hline
 & \frac{1471266399579}{7840856788654} & -\frac{4482444167858}{7529755066697} & \frac{11266239266428}{11593286722821} & \frac{1767732205903}{4055673282236}
\end{array}$$

**Implicit, Third-order ESDIRK3**

$$\begin{array}{c|cccccc}
0 & 0 & 0 & 0 & 0 & 0 & 0 \\[4pt]
\frac{1}{2} & \frac{1}{4} & \frac{1}{4} & 0 & 0 & 0 & 0 \\[4pt]
\frac{83}{250} & \frac{8611}{62500} & -\frac{1743}{31250} & \frac{1}{4} & 0 & 0 & 0 \\[4pt]
\frac{31}{50} & \frac{5012029}{34652500} & -\frac{654441}{2922500} & \frac{174375}{388108} & \frac{1}{4} & 0 & 0 \\[4pt]
\frac{17}{20} & \frac{15267082809}{155376265600} & -\frac{71443401}{120774400} & \frac{730878875}{902184768} & \frac{2285395}{8070912} & \frac{1}{4} & 0 \\[4pt]
1 & \frac{82889}{524892} & 0 & \frac{15625}{83664} & \frac{69875}{102672} & -\frac{2260}{8211} & \frac{1}{4} \\[4pt]
\hline
 & \frac{82889}{524892} & 0 & \frac{15625}{83664} & \frac{69875}{102672} & -\frac{2260}{8211} & \frac{1}{4}
\end{array}$$

**Implicit, Fourth-order ESDIRK4**

$$\begin{array}{c|cccccccc}
0 & 0 & 0 & 0 & 0 & 0 & 0 & 0 & 0 \\[4pt]
\frac{41}{100} & \frac{41}{200} & \frac{41}{200} & 0 & 0 & 0 & 0 & 0 & 0 \\[4pt]
\frac{2935347310677}{11292855782101} & \frac{41}{400} & -\frac{567603406766}{11931857230679} & \frac{41}{200} & 0 & 0 & 0 & 0 & 0 \\[4pt]
\frac{1426016391358}{7196633302097} & \frac{683785636431}{9252920307686} & 0 & -\frac{110385047103}{1367015193373} & \frac{41}{200} & 0 & 0 & 0 & 0 \\[4pt]
\frac{92}{100} & \frac{3016520224154}{10081342136671} & 0 & \frac{30586259806659}{12414158314087} & -\frac{22760509404356}{11113319521817} & \frac{41}{200} & 0 & 0 & 0 \\[4pt]
\frac{24}{100} & \frac{218866479029}{1489978393911} & 0 & \frac{638256894668}{5436446318841} & -\frac{1179710474555}{5321154724896} & -\frac{60928119172}{8023461067671} & \frac{41}{200} & 0 & 0 \\[4pt]
\frac{3}{5} & \frac{1020004230633}{5715676835656} & 0 & \frac{25762820946817}{25263940353407} & -\frac{2161375909145}{9755907335909} & -\frac{211217309593}{5846859502534} & -\frac{4269925059573}{7827059040749} & \frac{41}{200} & 0 \\[4pt]
1 & \frac{872700587467}{9133579230613} & 0 & 0 & \frac{22348218063261}{9555858737531} & -\frac{1143369518992}{8141816002931} & -\frac{39379526789629}{19018526304540} & \frac{32727382324388}{42900044865799} & \frac{41}{200} \\[4pt]
\hline
 & \frac{872700587467}{9133579230613} & 0 & 0 & \frac{22348218063261}{9555858737531} & -\frac{1143369518992}{8141816002931} & -\frac{39379526789629}{19018526304540} & \frac{32727382324388}{42900044865799} & \frac{41}{200}
\end{array}$$

**Implicit, Fifth-order ESDIRK5**

American Institute of Aeronautics and Astronautics

# References

[1]Bijl, H., Carpenter, M. H., Vasta, V. N., and Kennedy, C. A., "Implicit time integration schemes for the unsteady compressible Navier-Stokes equations: Laminar Flow," *Journal of Computational Physics*, Vol. 179, 2002, pp. 313–329.

[2]Kennedy, C. A. and Carpenter, M. H., "Additive Runge-Kutta schemes for convection-diffusion-reaction equations," *Applied Numerical Mathematics*, Vol. 44, No. 1-2, 2003, pp. 139–181.

[3]Dahlquist, G., "A special stability problem for linear multistep methods," *BIT*, Vol. 3, 1963, pp. 27–43.

[4]Wang, L. and Mavriplis, D. J., "Implicit solution of the unsteady Euler equations for high-order accurate discontinuous Galerkin discretizations," *Journal of Computational Physics*, Vol. 225, 2007, pp. 1994–2015.

[5]Venkataswaran, S., Deshpande, M., and Merkle, C. L., "The application of preconditioning to reacting flow computations," AIAA Paper 1995-1673-CP, 1995.

[6]Turkel, E., "Preconditioned methods for solving the incompressible and low speed compressible equations," *Journal of Computational Physics*, Vol. 72, 1987, pp. 277–298.

[7]Fiterman, A., Turkel, E., and Vatsa, V., "Pressure updating methods for the steady-state fluid equations," AIAA Paper 1995-1652-CP, 1995.

[8]Venkataswaran, S. and Merkle, C. L., "Analysis of preconditioning methods for the Euler and Navier-Stokes equations," VKI Lecture Series, von Karman Institute for Fluid Dynamics, Belgium, 1999, 1999.

[9]Venkataswaran, S. and Merkle, C. L., "Efficiency and accuracy issues in contemporary CFD algorithms," AIAA Paper 2000-2251, 2000.

[10]Sankaran, V., Merkle, C. L., Zeng, X., and Li, D., "Influence of large-scale pressure changes on preconditioned solutions at low speeds," *AIAA Journal*, Vol. 42, 2004, pp. 2490–2498.

[11]de B. Alves, L. S., "Dual time stepping with multi-stage schemes in physical time for unsteady low mach number compressible flows," VII de Primavera de Transição e Turbulência, Sept. 2010.

[12]de Medeiros, F. E. L. and de B. Alves, L. S., "Preconditioning methods for low mach number compressible flow simulations with an optimized pseudo speed of sound," 13th Brazilian Congress of Thermal Sciences and Engineering, Dec. 2010.

[13]Merkle, C. L. and Athavale, M., "A time accurate unsteady incompressible algorithm based on artificial compressibility," AIAA Paper 1987-1137, 1987.

[14]Charney, J. G., Fjørtoft, R., and von Neumann, J., "Numeric integration of the barotropic vorticity equation," *Tellus*, Vol. 2, 1950, pp. 237–254.

[15]Prothero, A. and Robinson, A., "On the stability and accuracy of one-step methods for solving stiff systems of ordinary differential equations," *Mathematics of Computation*, Vol. 28, 1974, pp. 145–162.

[16]Lele, S. K., "Compact finite difference schemes with spectral-like resolution," *Journal of Computational Physics*, Vol. 103, 1992, pp. 16–42.

[17]Gaitonde, D. V. and Visbal, M. R., "Padé-type higher-order boundary filters for the Navier-Stokes equations," *AIAA Journal*, Vol. 38, 2000, pp. 2103–2112.

[18]Edoh, A. K., Karagozian, A. R., Sankaran, V., and Merkle, C. L., "Comparison of artificial dissipation and filtering schemes for time-accurate simulations," AIAA Paper 2015-0284, 2015.

[19]Butcher, J. C., *Numerical Methods for Ordinary Differential Equations*, Wiley, 2003.